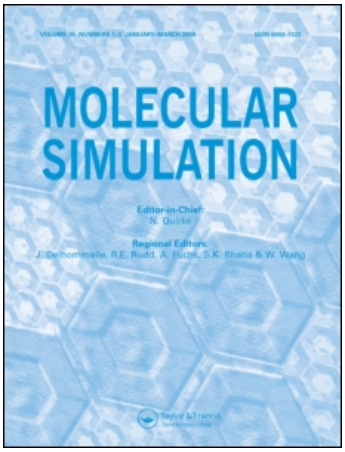

Molecular Simulation
Publication details, including instructions for authors and subscription information:
http://www.informaworld.com/smpp/title~content=t713644482

A semi-empirical molecular orbital study of freestanding and fullerene-encapsulated Mo nanoclusters

James A. Elliott[a]; Yasushi Shibuta[b]
[a] Department of Materials Science and Metallurgy, University of Cambridge, Cambridge, UK [b] Department of Materials Engineering, The University of Tokyo, Tokyo, Japan

To cite this Article Elliott, James A. and Shibuta, Yasushi(2008) 'A semi-empirical molecular orbital study of freestanding and fullerene-encapsulated Mo nanoclusters', Molecular Simulation, 34: 10, 891 — 903
To link to this Article: DOI: 10.1080/08927020802258724
URL: http://dx.doi.org/10.1080/08927020802258724

Molecular Simulation
Vol. 34, Nos. 10–15, September–December 2008, 891–903

Taylor & Francis
Taylor & Francis Group

A semi-empirical molecular orbital study of freestanding and fullerene-encapsulated Mo nanoclusters

James A. Elliott[a]* and Yasushi Shibuta[b]

[a]*Department of Materials Science and Metallurgy, University of Cambridge, Cambridge, UK;* [b]*Department of Materials Engineering, The University of Tokyo, Tokyo, Japan*

(*Received 9 March 2008; final version received 9 June 2008*)

Nanoscopic transition metal clusters are widely used in the catalytic growth of carbon nanotubes (CNTs) synthesised using a chemical vapour deposition process. It is known that addition of oxygen and heavier chalcogens such as sulphur can both increase CNT growth rate and maximum length, and also promote selective growth of single and double wall CNTs. We describe results of semi-empirical molecular orbital calculations, using the AM1* Hamiltonian as implemented in the VAMP module of Materials Studio®, of both freestanding and fullerene-encapsulated molybdenum (Mo) clusters, which show that metal clusters above a critical size cause the formation of defects by opening of hexagon–hexagon (6–6) carbon bonds that lead eventually to a splitting open of the fullerene cage. Furthermore, we demonstrate that the addition of oxygen, nitrogen and sulphur to the molybdenum cluster cause changes to its electronic and geometric structure. Our simulations clearly demonstrate the strong interaction of the metal catalyst particle with the fullerene cap of a growing CNT, which may affect one or more stages of carbon incorporation into CNTs according to the commonly accepted vapour–liquid–solid growth model, although the precise mechanism requires further investigation.

Keywords: semi-empirical molecular orbital theory; AM1*; molybdenum nanoclusters; carbon nanotube synthesis; chemical vapour deposition

1. Introduction

The development of large-scale, high-purity production methods for carbon nanotubes (CNTs) is highly desirable for further increasing the practical applications of these fascinating materials. In addition to the previously known laser furnace [7] and arc discharge techniques [8], catalytic chemical vapour deposition (CCVD) methods [1–4,9–12] have been widely pursued as a potential low cost, large-scale production method. In earlier versions of this technique, such as the high-pressure carbon monoxide method [9], floating catalysts were used during the CVD process. However, more recently, a high-purity technique for production of vertically aligned single-walled CNTs on a quartz substrate was developed using a supported catalyst [10], which was followed by a later refinement by the addition of water, resulting in very long (millimetre-thick) nanotube forests [11], and later termed 'super-growth' [13]. Koziol et al. [14] recently reported mechanical property data from high performance CNT fibres, in which the addition of sulphur was critical for promoting the formation of thin walled nanotubes on the catalyst surface [3].

In order to achieve higher efficiencies for the CCVD method, and a greater degree of control over the type and structure of CNTs produced, the role of catalyst metals has been widely studied [12,15]. It is well known that the catalytic metals are essential for synthesis of single wall CNTs (SWCNTs). The mechanism by which this occurs is commonly thought to be according to the vapour–liquid–solid (VLS) model [16,17], which involves the following steps: adsorption and decomposition of the carbon source molecules at the surface of the catalytic metal, followed by diffusion of the carbon atoms within the particle, and their segregation and graphitisation once the metal cluster is saturated with carbon. There exist an abundance of transmission electron microscope images of the catalytic metals attached to the tip or root of SWCNTs [18,19] which support such a mechanism. Furthermore, studies of the formation process by molecular dynamics (MD) simulation [20,21] are also consistent with the VLS model. It is therefore plausible that the action of additives such as oxygen and sulphur, which are a prerequisite for super-growth [13] or rapid production of fibres [3], is to affect one or more stages of carbon incorporation into CNTs according to the VLS model.

At present, it is not yet clear which metal is most suitable as a catalyst of CNT growth, although various transition metals (including iron, cobalt, nickel and molybdenum) and their alloys are commonly used. For example, Herrera et al. [22] found that the selectivity

*Corresponding author. Email: jae1001@cam.ac.uk

ISSN 0892-7022 print/ISSN 1029-0435 online

DOI: 10.1080/08927020802258724
http://www.informaworld.com

of Co–Mo catalysts towards formation of SWCNTs depended on stabilisation of Co species in a nonmetallic state, resulting from an interaction with Mo that is a function of the Co:Mo ratio. On the other hand, Lan et al. [23] claimed that Mo may not in fact be necessary for the formation of SWNCTs, which they produced using Co alone. The catalytic activities of various transition metals in the formation of SWCNTs by a laser-furnace technique were compared [24], resulting in three criteria which could be used to determine a 'better' catalyst: graphitisation ability, low solubility in carbon, and stable crystallographic orientation on graphite. Flahaut et al. [25] found that a variation in the proportion of Mo with respect to Co in a mixed (Mg, Co and Mo) oxide catalyst had an influence on the yield, structure and purity of tubes produced. Hu et al. [26] studied the morphology and chemical state of Co–Mo catalysts using transmission electron microscopy and X-ray photoelectron spectroscopy, and found that particles composed of Co molybdates and metallic Co are important for the promotion of SWCNT growth. Recently, a combinatorial method for examining the best concentration ratio of Mo–Co binary metal nanoparticles [27], or Fe/Al_2O_3 catalysts [28] were investigated, and millimetre-thick forests of nanotubes were produced [28].

In parallel to the experimental approaches, numerical simulations have contributed to the interpretation of the role of the catalytic metals during CNT growth. The CNT formation process has been investigated by various types of calculation, including: classical MD [20,21,29,30], *ab initio* MD [31,32], *ab initio* molecular orbital (MO) methods [33] and tight-binding Monte Carlo [32,34]. In general, each level of the calculation has its own advantages and disadvantages: *ab initio* methods have high chemical precision and few free parameters, but the time and size scales of such simulations are extremely restricted by their computational complexity [35]. Hence, an appropriate method should be selected for the purpose of the calculation in every case. One way of overcoming the computational limit is to develop a multi-scale modelling approach for understanding the formation process of CNTs [36]. However, it is difficult to capture the entire process of CNT growth, from carbon source molecules to a forest of cylindrical tubes.

Due to their important role in CNT growth, among other reasons, the thermodynamic stability of different types of catalytic metal nanoclusters, including the noble metals Au [37,38] and Ag [39], and various transition metals [40–43], have been studied using an atomistic modelling approach. The general issues of how structural properties of nanoclusters depend on their energetics, thermodynamics and kinetic effects were recently reviewed by Baletto and Ferrando [44] and, for transition metal clusters in particular, Alonso [45] has summarised their electronic, magnetic and structural properties. Therefore, we shall not give a detailed discussion here; however, it suffices to say that even using very simple empirical pair potentials (e.g. Lennard-Jones [46]) or embedded atom models (e.g. Sutton–Chen [47] and Gupta [48]), finding the global minimum energy configuration for a pure metal nanocluster of more than 100 atoms is an extremely challenging problem. For *ab initio* methods, and alloyed systems, an exhaustive search is therefore out of the question. Nevertheless, there are a range of general structural motifs, some with only short-range order (e.g. icosahedral or decahedral clusters) and some with long-range order (e.g. closed-packed clusters) which occur regularly in a wide range of systems due to stabilisation either by geometric or electronic effects [44], leading to certain 'magic sizes' predominating in distributions of clusters. In the case of clusters of transition metals typically used for catalysed CNT growth, in which the d electrons in unfilled shells are localised, geometric stabilisation is the dominant effect [45].

The properties of the Mo and Mo-S nanoclusters have been examined previously using *ab initio* calculations, and their structural stability is discussed in Refs. [49–56]. Most studies used density functional theory (DFT) with a generalised gradient approximation for the exchange-correlation functional, and focused on the role of MoS_x clusters in heterogeneous catalysis. The main conclusion of relevance to current work is that the lowest energy structures tend to have a metal core with sulphur atoms at the surface. However, in general, the size of the clusters was too small (typically from 1 to 10 Mo atoms, although Li and Galli recently presented results on triangular $(MoS_2)_n$ platelets with n up to 78 [56]) to discuss the role of the Mo during CNT growth due to the computational demands of DFT. For this reason, a semi-empirical MO (SEMO) calculation using the AM1* Hamiltonian was employed in this study in order to investigate the stability of freestanding and fullerene-encapsulated Mo clusters. A more detailed justification for the choice of SEMO methods is given in Section 2, and the rest of the paper is structured as follows. First, the energy and structure of the freestanding clusters of Mo_n and $Mo_{(n-x)}X_x$ (with X: O, S, N) are examined. Then, the energy and structure of fullerene-encapsulated $Mo_n@C_{180}$ clusters are investigated, focusing on the defect formation and breakup of fullerene. Finally, we conclude with a discussion of the effect of sulphur addition in $Mo_{(52-x)}S_x@C_{180}$ encapsulated molybdenum sulphide clusters.

2. Computational methodology

SEMO methods based on the neglect of diatomic differential overlap (NDDO) approximation have been widely used on small and medium-sized organic molecules after the publication in 1977 of the first

NDDO-type method: MNDO (standing for modified neglect of diatomic overlap) by Dewar et al. [57] for molecules containing hydrogen, carbon, nitrogen and oxygen [58]. Since then, more sophisticated Hamiltonians based on NDDO, such as AM1 and PM3, have extended coverage of SEMO methods to all main group elements, and a recent review summarises the variety of applications and successes of these techniques [59]. However, it is important to realise that the degree of empiricism inherent in SEMO methods, which are based on Hartree-Fock (HF) theory, is quite different to that of so-called 'empirical' force field models, such as those for metal clusters mentioned in the preceding section. NDDO neglects only differential overlap between atomic orbitals on different atoms, and retains all two-electron, two-centre integrals on the same atoms [35]. To compensate for this neglect, MNDO introduces parametric expressions for the two-centre integrals, which are derived from charge distributions around the interacting atoms. The parameters in these expressions are determined by fitting to heats of formation, molecular geometries, ionisation potentials and dipole moments of a wide range of molecules. In this way, it is possible to compensate for deficiencies such as neglect of electronic correlation and the simplifying assumptions of NDDO. SEMO models are therefore usually transferable between different types of molecule, provided that representative structures have been included in the training data set. By contrast, empirical force field models are usually based on much more severe semi-classical approximations (such as bead-spring or mean-field representations) and must be carefully refitted for each new type of system or change of atomic composition. SEMO methods therefore have the advantage of having fewer variable parameters, and can yield results with precision comparable to some post-HF *ab initio* methods with a much lower computational cost [60]. In Section 3.1, we compare SEMO results for a Mo cluster (based on AM1*, described below) directly with DFT using a hybrid exchange-correlation functional (B3LYP) [61,62] with a minimal basis set.

Until quite recently, NDDO-type SEMO calculations based on MNDO were restricted to main group elements containing only s and p electrons, although older types of SEMO methods had been used for calculating spectroscopic properties [63] and geometries [64] of transition metal compounds. Voityuk and Rösch were the first to describe an extension of AM1 to d orbitals, which they called AM1/d, and recently reported parameters for Mo [65]. Their approach was based on an extended multipole–multipole interaction scheme [64] and the introduction of two bond-specific parameters for Mo in the core–core repulsion term [65]. The AM1/d scheme has the advantage that results obtained for non-transition-metal atoms are identical to those for the original AM1 method, while the former is additionally able to reproduce chemical properties of complex organometallic and bioinorganic compounds of Mo with high precision [65]. The Mo parameters in AM1/d were later incorporated in a slightly modified form by the Clark group into their AM1* Hamiltonian [5,66], which uses a distance-dependent core–core repulsion for some interactions. The same group then later reported AM1* parameters for Al, Si, Ti and Zr [67]. The AM1* Hamiltonian is implemented in the SEMO software package VAMP, now part of Materials Studio® (MS) from Accelrys, San Diego, CA, USA which, at the time of writing (MS version 4.2), contains parameters for the following elements: H, C, N, O, F, Al*, Si*, P*, S*, Cl*, Ti*, Cu*, Zn*, Zr* and Mo*, with the asterisked elements containing parameter sets that include d orbitals. In this way, it has been possible to use AM1* to study Mo clusters in contact with C, O, S and N, which are of relevance to CNT production via a CCVD process, without further parameterisation. Optimised geometries and single point energies were computed using the standard eigenvector following (EF) and self-consistent field (SCF) convergence algorithms in VAMP [6]. In future, with the recent publication by Stewart [68] of NDDO-type parameter sets including Co, Ni and Fe as part of the PM6 Hamiltonian (an extension of PM3), it will be possible in principle to extend this work to comparative studies of other transition metal elements (and their alloys) typically used in the CCVD processes described earlier.

Before describing the results obtained with AM1* on Mo-based clusters, we will briefly remark on one further simplification made in this study: the use of spin-restricted (RHF) methods for all calculations. Since the ground state electronic configuration of Mo is $[Kr]5s^1 4d^5$, it may generally be expected that the unpaired d electrons will give rise to a net magnetic moment for a Mo cluster. For small clusters, interactions between the electronic spins of adjacent atoms can be very significant, although the magnetic moments for typical transition metal clusters (such as Fe, Co and Ni) are known to converge to their bulk values for sizes larger than a few hundred atoms [45]; this effect can be understood in terms of the local under-coordination of surface atoms in the smaller clusters. Although it is straightforward to express HF theory, and therefore SEMO methods, in a spin-polarised framework, it was found at a very early stage of this work that spin-unrestricted (UHF) calculations on pure Mo clusters resulted in very high values of the total electronic spin. In order to avoid the effects of spin contamination, in which contributions from excited states are mixed with the ground state wavefunction, it is conventional to require that the expectation value of total spin operator $\langle S^2 \rangle$ lies within 10% of $S(S+1)$, where S is the total electronic spin [69]. Since the spin state of the Mo clusters is, in general, unknown *a priori*, it is difficult to eliminate the effects of spin contamination of the ground state wavefunction, and hence to avoid any systematic errors due to mixing with

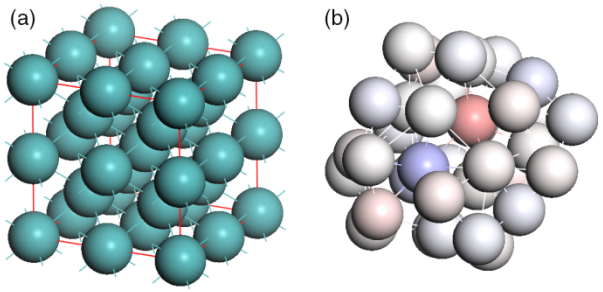

Figure 1. Mo_{35} nanocluster: (a) initial configuration generated from $2 \times 2 \times 2$ b.c.c. supercell and (b) the resulting structure optimised at RHF/AM1* level without periodic boundaries or symmetry constraints. Mo atoms in (b) are coloured (online) according to their Mulliken charges: red − ve, blue + ve.

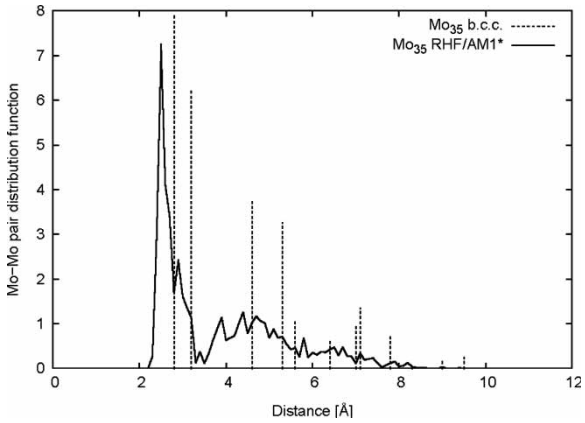

Figure 2. Mo–Mo pair distribution functions for the Mo_{35} structures shown in Figure 1: dashed line, Figure 1(a); solid line, Figure 1(b).

exited states using UHF. Therefore, all optimisations were carried using RHF, under the assumption that the electron spins are paired. This is possible in general for all Mo_n and $Mo_{(n-x)}X_x$ clusters, where $X = \{O, N\}$, since each atom has an even number of valence electrons, but where $X = \{N\}$, nitrogen atoms were added in pairs in order to maintain an even total number of electrons. Under this assumption, the effects of magnetism are thus ignored as a first approximation. However, previous DFT calculations by Murugan et al. [55] on small Mo-S clusters have shown that structural changes due to spin polarisation are small.

3. Results

3.1 *Freestanding Mo_n clusters*

The first attempts to build stable Mo_n cluster were based on an initial configuration consisting of a $2 \times 2 \times 2$ supercell for bulk crystalline Mo (taken from the Materials Studio structural database, space group Im–3m, lattice parameter $a = 3.1469$ Å), as shown in Figure 1(a). The periodic boundary conditions were then removed from the supercell to create a freestanding b.c.c. cluster containing 35 atoms. Figure 1(b) shows the resulting structure after geometry optimisation at the RHF/AM1* level using VAMP (with SCF tolerance 5×10^{-7} eV atom^{-1}, and r.m.s. force convergence 0.1 kcal mol^{-1} Å^{-1}), with atoms colour-coded (online) according to their Mulliken charges. The total decrease in energy was − 123.4 eV, corresponding to − 3.53 eV atom^{-1}. It is clear that the most stable structure of the Mo_{35} cluster is amorphous, in contrast to the bulk crystalline form.

The Mo–Mo pair distribution functions for the crystalline and amorphous clusters of Mo_{35} given in Figure 1 are shown in Figure 2 (normalised to bulk coordination number for bulk crystal of 8). They confirm that the structural order in the amorphous particle (Figure 1(b)) is only very short-ranged, and also show that there is a small decrease in the nearest neighbour separation due to a decrease in local coordination of Mo atoms at the edge of the cluster as compared to the bulk. This is a well-known effect in simulations for metal clusters using many-body potentials [29].

In order to check the reliability of the AM1* method for calculating the geometry and energies of Mo clusters in this study, the RHF/AM1* cluster geometry shown in Figure 1(b) was compared against DFT calculations using the B3LYP hybrid functional calculated with Gaussian03 [70]. Due to the computational demands of the DFT calculation, which took nearly two weeks of CPU time on a quad-processor Itanium2 machine, it was only possible to re-optimise the structure using a minimal basis set (STO-3G). A comparison of the AM1* and B3LYP/STO-3G optimised clusters is shown in Figure 3. The change in the structure after re-optimisation with DFT is only very

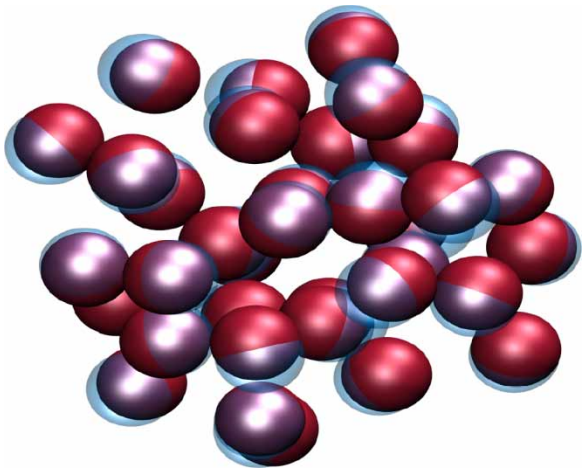

Figure 3. Aligned structures of Mo_{35} nanocluster optimised with AM1* (red (online), solid) and B3LYP/STO-3G (blue (online), transparent). The r.m.s.d. between the two structures is 0.22 Å/atom (evaluated with Kabsch method).

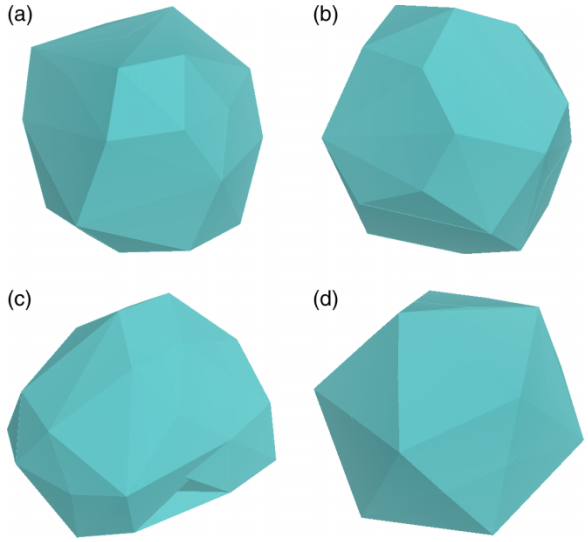

Figure 4. Comparison of optimised Mo_n cluster structures generated by RHF/AM1* optimisation after sequential addition: (a) Mo_{35}, and (c) Mo_{55}, and starting at global minimum for Gupta potential: (b) Mo_{35}, and (d) Mo_{55}. Representation is polyhedral, with Mo atoms (not shown) at the vertices.

slight, with a r.m.s. displacement of 0.22 Å atom^{-1}, and the difference in energy between the structures is $\Delta E = 205$ meV atom^{-1} (evaluated at the B3LYP/STO-3G level). Although this is by no means a conclusive test of the reliability of the AM1* method for our given application, it nonetheless adds confidence to the validation work carried out previously for organometallic compounds [5,65]. Furthermore, since the CPU time required to carry out the SEMO calculation was a factor of approximately 10^3 lower than required to achieve the DFT result, the latter technique is still impractical for a systematic study such as undertaken here.

Attempts to build larger Mo_n particles, with $n > 35$, using a similar method as described above for Mo_{35} proved difficult due to convergence failure of the SCF calculation. Instead, an alternative method was used in which individual Mo atoms were added sequentially to the previously optimised clusters, before re-optimising at RHF/AM1* level. In this way, clusters of arbitrary size can be generated, although the process is rather slow, and the question naturally arises as to how close these structures are to the global energy minimum for clusters of that size. It must be emphasised that, in this study, the aim was not to carry out an exhaustive search for the global minimum. Nevertheless, as a further test of the confidence of the RHF/AM1* method for calculating viable cluster structures, and to give some indication of how close these structures might be to the global energy minimum, we compared optimised structures calculated for Mo_{38} and Mo_{55} clusters generated by sequential addition to those relaxed from coordinates of the global optima, taken from the Cambridge Cluster Database [71], computed using the Gupta potential for Co [48] (with interatomic distances rescaled to bulk value for Mo). The reason for choosing $n = 38$ and 55 is that these are geometrically magic numbers, corresponding to the truncated octahedron and Mackay icosahedron structures, respectively. Similar structures were also predicted for both 12-6 Lennard-Jones [46] and Ni (modelled by 9-6 Sutton–Chen) [47] clusters of equivalent size, so it appears that they are global minima across a wide range of systems. Hence, there is a good chance that the global energy minimum at the RHF/AM1* level, or a structure very close to it, can be found by the straightforward EF algorithm using VAMP from these initial coordinates.

Figure 4 shows a comparison of RHF/AM1* optimised Mo_{38} clusters resulting from sequential addition, in Figure 4(a), and from the Gupta global minimum, in Figure 4(b). The overall shape of the Mo_{38} clusters is qualitatively similar, although the surface facets in Figure 4(a) are not as well-defined for the cluster made by sequential addition, and there is some distortion preferred in Figure 4(b) even compared to a perfect truncated octahedron. The overall energy difference is $\Delta E = 1.860$ eV, corresponding to 48.9 meV atom^{-1} in favour of the structure in Figure 4(b), which is approximately twice k_BT at 300 K. Therefore, it is reasonable to suppose that the structure in Figure 4(a) may be one of a family of structures which are all thermally indistinguishable from the global minimum. Figure 4(c),(d) shows equivalent structures for Mo_{55}, made by sequential additional and relaxation from Gupta global minimum, respectively. In this case, the structures differ qualitatively in appearance, with the cluster made by sequential addition, shown in Figure 4(c), being less spherical. However, the difference in energies is still only $\Delta E = 5.412$ eV, corresponding to 98.4 meV atom^{-1} in favour of the structure in Figure 4(d). We conclude that although optimised structures formed by sequential addition are not in general global minima, they lie very close in energy to more regular structures that could be global minima, even for clusters that differ markedly in shape. Of course, only an exhaustive search would establish with certainty the global minimum structure, and this was not attempted here.

3.2 *Freestanding Mo-X clusters*

Having established a suitable methodology for generating freestanding Mo_n clusters, it was subsequently possible to investigate the effects of addition by random substitution of oxygen and sulphur atoms, and nitrogen dimers, to Mo clusters with a fixed total number of atoms. We adopt the nomenclature $Mo_{(35-x)}X_x$, where X = {S, O, N} and x is the number of non-metal atoms. Each non-metal atom

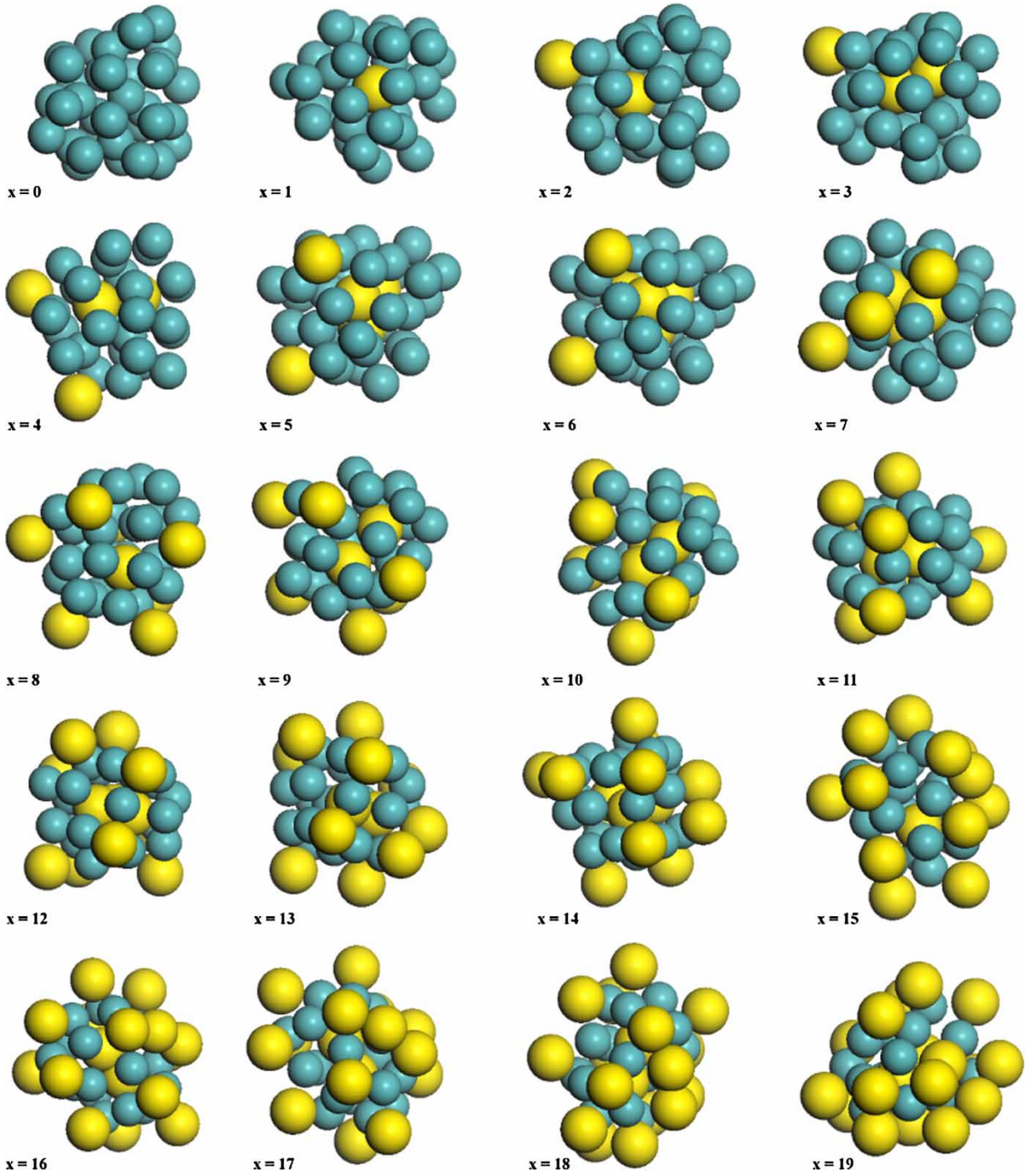

Figure 5. $Mo_{(35-x)}S_x$ nanoclusters optimised at RHF/AM1* level. Mo atoms are shown in turquoise (online), and sulphur atoms in yellow (online).

substitution was made by transforming one Mo atom chosen at random, and then re-optimising the cluster geometry. As in the case of pure Mo clusters studied in Section 3.1, no attempt was made to make an exhaustive search for global minimum energy, but it was presumed that the resulting structures would be representative of realistic cluster geometries. Figure 5 shows a series of optimised structures for $Mo_{(35-x)}S_x$ for $0 \leq x \leq 19$, and similar series were generated for O and N substitutions. Although it is difficult to draw any definite conclusions from just a qualitative inspection of the structures in Figure 5, an interesting event occurs in going from $x = 7$ to $x = 8$: a tetrahedral cluster of four S atoms in the centre of $x = 7$ cluster is disrupted by the addition of a further S

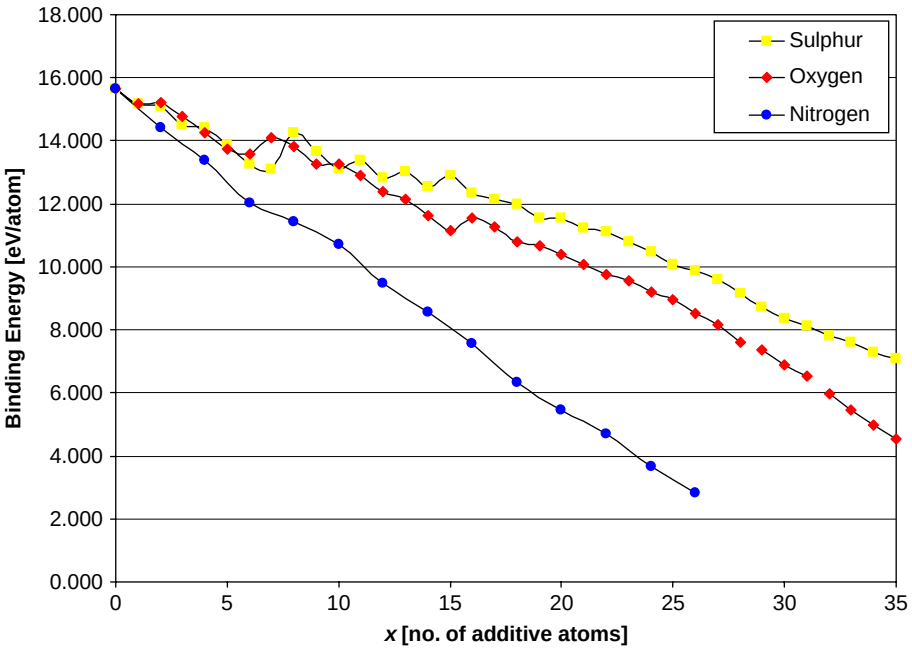

Figure 6. Behaviour of binding energy for $Mo_{(35-x)}X_x$ clusters as a function of non-metal additive and number of additive atoms.

atom, resulting in the majority of S atoms moving to the surface of the $x = 8$ cluster with a corresponding drop in the heat of formation. This behaviour is similar to that found for small Mo-S particles by Murugan et al. [55], who reported that lowest energy structures tended to have a metal core with sulphur atoms at the surface.

In order to assess quantitatively the stability of $Mo_{(35-x)}X_x$ clusters as a function of their stoichiometry, we define a binding energy per atom, B.E.$^{\text{free}}$, according to Equation (1):

$$\text{B.E.}^{\text{free}} \equiv \frac{xE^{\text{AM1}^*}(\text{X}) + yE^{\text{AM1}^*}(\text{Mo}) - E^{\text{AM1}^*}(\text{X}_x, \text{Mo}_y)}{x + y}, \tag{1}$$

where x and y are number of X and Mo atoms, respectively (with total number of atoms $n = x + y$), and $E^{\text{AM1}^*}(\text{X})$ and $E^{\text{AM1}^*}(\text{Mo})$ are the energies of isolated atoms of X and Mo, respectively, and $E^{\text{AM1}^*}(\text{X}_x,\text{Mo}_y)$ is the total energy of RHF/AM1* geometry optimised cluster.

The behaviour of B.E.$^{\text{free}}$ for clusters of $n = 35$ atoms with $\text{X} = \{\text{S}, \text{O}, \text{N}\}$ is shown as a function of x in Figure 6. In all cases, the B.E.$^{\text{free}}$ of the Mo_{35} cluster is reduced from an initial value of 15.658 eV atom^{-1} (or 5.062 eV bond^{-1} according to Mayer bond orders) by the substitution of non-metal atoms. This is expected due to the disruption of metallic bonding between the Mo atoms. In the case of N, the rate of decrease is highest and monotonic with increasing number of atoms substituted. However, for S and O substitution, the rate of decrease is less rapid, and non-monotonic. In particular, for S substitution, the expulsion of S atoms to the surface of the $x = 8$ cluster (as shown in) corresponds to a small local rise in the cluster stability. A similar transition occurs for O substitution when $x = 7$. These may be interpreted as magic compositions for Mo-X clusters, which are stabilised by surface addition of non-metal additive, although an exhaustive search of cluster geometries for each composition would be required to establish this definitively. There are smaller subsidiary fluctuations in B.E.$^{\text{free}}$ curve for both S and O-substituted clusters between $9 \leq x \leq 16$, but for $x > 16$ both curves become monotonically decreasing as the non-metal atoms dominate behaviour of cluster. For cluster with a larger total number of atoms, it may be possible to observe magic behaviour for a greater number of substituted atoms. In summary, calculations on freestanding Mo-X clusters show preferential segregation of S and O to the surface of Mo clusters for certain compositions, which is consistent with previous DFT studies on small clusters [55] and experimental studies of Fe-catalysed CNT growth in which sulphur-rich layer was seen to form at the surface of the catalyst particle [72]. We next describe the behaviour of fullerene-encapsulated clusters.

3.3 *Endohedral $Mo_n@C_{180}$*

Even using SEMO techniques, the size of system required for simulating a metal cluster interacting with a graphene sheet presents a formidable challenge, and therefore a more simplified model is required. Instead, the free-standing Mo_n clusters studied in Section 3.1 were

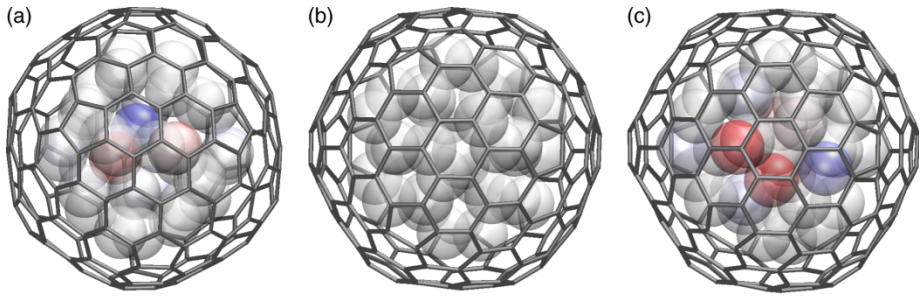

Figure 7. Endohedral fullerene Mo_n clusters: (a) $Mo_{35}@C_{180}$, (b) $Mo_{36}@C_{180}$ and (c) $Mo_{37}@C_{180}$. Mo atoms are represented by semi-transparent spheres, coloured (online) according to their Mulliken charges (red being negative, blue being positive) with ranges set the same for each image.

encapsulated by a spherical fullerene molecule, which has the advantage of being highly symmetrical (i.e. no periodic boundaries or dangling bonds), and whose properties are already well known. Whilst buckminsterfullerene, C_{60}, itself is too small to encapsulate anything larger than isolated atoms [73–78], there are other related structures sufficiently large to completely contain a Mo_{35} cluster; we chose the I_h isomer of C_{180} that satisfies the isolated pentagon rule. Of course, due to its closed π-system, C_{180} is more stable than a graphene sheet of equivalent size but by changing the size and composition of the encapsulated cluster, we were able to observe the effects of perturbing the C_{180} ground state and thereby draw inferences about the nature of interaction between the cluster and fullerene. We adopt the standard nomenclature for endohedral fullerenes of $X@C_{180}$, where X denotes the chemical formula of the encapsulated cluster.

Figure 7 shows a set of visualisations, aligned and rendered using the visual molecular dynamics (VMD) package [79], for RHF/AM1* optimised geometries of $Mo_n@C_{180}$ nanoclusters, where $n = 35–37$. The Mo atoms are represented by semi-transparent spheres, coloured (online) according to their Mulliken charges (with red being negative, blue being positive) and the colour ranges are identical for each image. It is possible to discern a general trend of increasing polarisation in the Mo_n cluster, which coincides with a slight distortion of the C_{180} structure and a decrease in the calculated C_{180} band gap, indicating that there is increasing charge transfer from the cluster to the C_{180} π-system as the cluster becomes larger. In Figure 8, the RDFs show a slight expansion of Mo–Mo distance in $Mo_{35}@C_{180}$ compared to a freestanding Mo_{35} cluster, again consistent with there being charge transfer from the Mo_n cluster to the fullerene molecule.

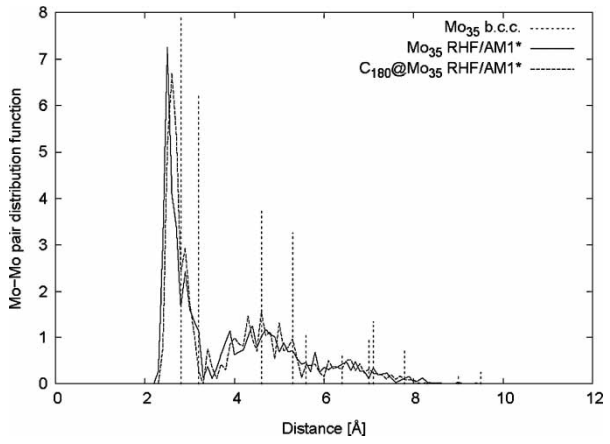

Figure 8. Mo–Mo pair distribution functions for the freestanding Mo_{35} cluster (shown in Figure 1(a)) and the $Mo_{35}@C_{180}$ endohedral structure (shown in Figure 7(a)). The distribution for bulk b.c.c. Mo is also included for comparison.

As the size of the Mo cluster was increased beyond $n = 37$ by sequential addition, as described in Section 3.1, the cluster polarisation and strain in the C_{180} molecule were further increased, resulting in the formation of defects in the fullerene structure for $n \geq 44$. Figure 9 shows a set of visualisations, aligned and rendered using the VMD package [79], for RHF/AM1* optimised geometries of $Mo_n@C_{180}$ nanoclusters, where $n = 44–53$, showing formation of first fullerene defect for $Mo_{44}@C_{180}$, a second defect for $Mo_{51}@C_{180}$ and finally rupture of fullerene cage structure for $Mo_{53}@C_{180}$. The defects observed in Figure 9(a),(b) are both of the 6–6 type, denoting the breakage of bonds between adjacent hexagons in the fullerene cage. This is consistent with the general observation that they are more reactive in chemical processes than 5–6 bonds between pentagons and hexagons, for example in the oxidative etching of CNTs [80]. It is interesting to note that the rupture appears to originate at the second defect site (Figure 9(b), yellow (online)), while the original defect site (Figure 9(a)–(b), green (online)) heals after the rupture has occurred (Figure 9(c)). It was also found that reducing the size of the Mo cluster after the formation of defects caused them to heal.

In order to study the interaction of Mo nanocluster and fullerene more quantitatively, we define of two types of binding energy: encapsulated cluster binding energy, $B.E._{endo}$ (Equation (2)), taking into account atomic decomposition of metal cluster only, and the total encapsulated cluster binding energy, $B.E._{endo}^{\prime}$ (Equation

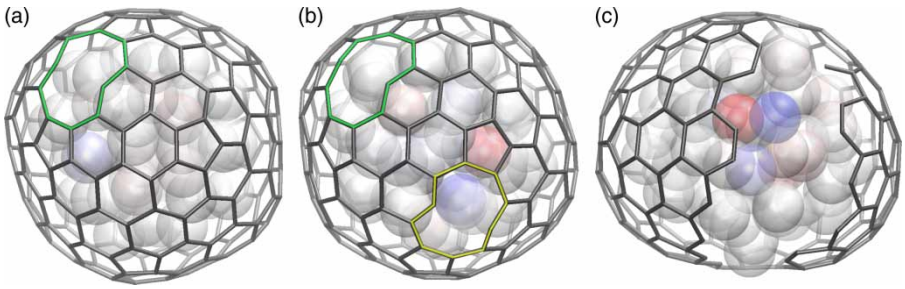

Figure 9. RHF/AM1* optimised geometries of endohedral fullerene Mo_n clusters: (a) $Mo_{44}@C_{180}$, (b) $Mo_{51}@C_{180}$ and (c) $Mo_{53}@C_{180}$. Mo atoms are represented by semi-transparent spheres, coloured (online) according to their Mulliken charges (red being negative, blue being positive) with ranges set the same for each image. Fullerene defects in (a) and (b) are highlighted in green and yellow, and full opening of fullerene cage is observed in (c), with bonding to Mo atoms (which terminate the dangling bonds) not shown for clarity.

(3)), taking into account total atomic decomposition of all components. The analytical expressions are given by:

$$\text{B.E.}_{\text{endo}} \equiv \frac{E^{\text{AM1}^*}(\text{C}_{180}) + nE^{\text{AM1}^*}(\text{Mo}) - E^{\text{AM1}^*}(\text{Mo}_n@\text{C}_{180})}{n}, \tag{2}$$

$$\text{B.E.}'_{\text{endo}} \equiv \frac{E^{\text{AM1}^*}(\text{C}'_{180}) + nE^{\text{AM1}^*}(\text{Mo}) - E^{\text{AM1}^*}(\text{Mo}_n@\text{C}_{180})}{n}, \tag{3}$$

where n are the number of Mo atoms in the encapsulated cluster, $E^{\text{AM1}*}(\text{C}_{180})$ and $E^{\text{AM1}*}(\text{Mo})$ are the energies of an isolated C_{180} molecule and Mo atom, respectively, and $E^{\text{AM1}*}(\text{Mo}_n@\text{C}_{180})$ is the total energy of RHF/AM1* geometry optimised endohedral cluster. $E^{\text{AM1}*}(\text{C}'_{180})$ is the energy of the strained C_{180} molecule calculated in isolation from the encapsulated cluster, but without further optimisation.

The difference between the two quantities given by Equations (2) and (3) is that $\text{B.E.}_{\text{endo}}$ does not take into account the strain energy induced in C_{180} due to expansion of the cluster, whereas $\text{B.E.}'_{\text{endo}}$ does. Figure 10 shows the behaviour of $\text{B.E.}_{\text{endo}}$ and $\text{B.E.}'_{\text{endo}}$, calculated as a function of the number of cluster atoms. Both quantities show an increase of approximately 0.75 eV atom^{-1} at the point of fullerene breakage ($n = 53$) but are relatively unchanged by formation of isolated 6–6 defects (at $n = 44$, 51). The general trend is for $\text{B.E.}_{\text{endo}}$ to decrease between $n = 39$ until the point of breakage ($n = 53$) which, by comparison with curve for $\text{B.E.}'_{\text{endo}}$ that increases monotonically, can be seen to be due to a build up of strain energy in the fullerene cage. After opening of the

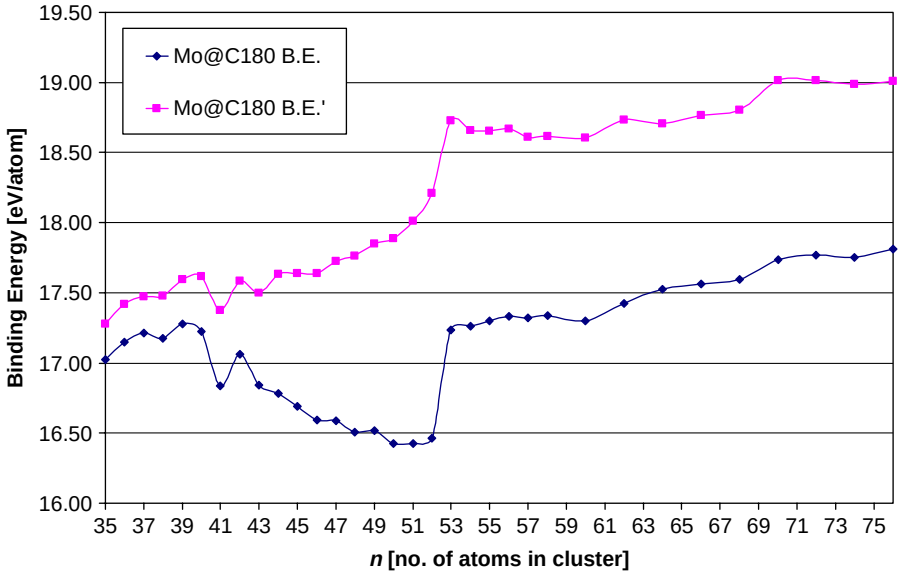

Figure 10. Binding energies of $Mo_n@C_{180}$ endohedral clusters, $\text{B.E.}_{\text{endo}}$ and $\text{B.E.}'_{\text{endo}}$, defined by Equations (2) and (3), as a function of the number of cluster atoms.

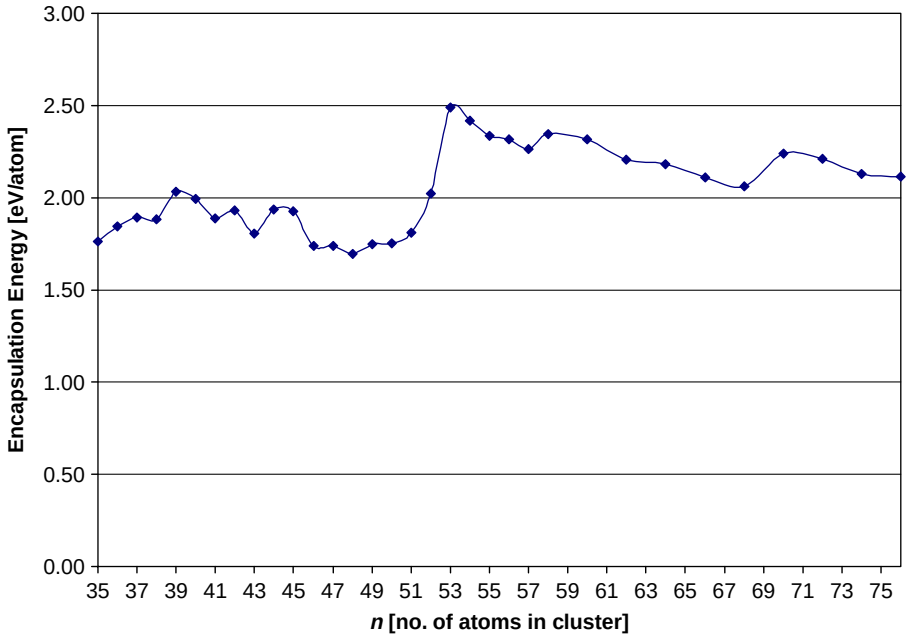

Figure 11. Encapsulation energies of $Mo_n@C_{180}$ endohedral clusters, E.E., defined by Equation (4), as a function of the number of cluster atoms.

fullerene, the binding energies rise steadily, showing the stabilising influence of the d electrons in the Mo cluster on the broken π-system of the fullerene.

In order to separate the effects of cluster encapsulation from changes in binding energy, we define cluster encapsulation energy, E.E. (Equation (4)), which only involves only dissociation of the strained C_{180} and Mo_n cluster. As shown in Figure 11, the E.E. changes only very slightly for $n > 35$, except for a small discrete jump around the breakage point ($n = 53$). Nevertheless, in all cases, encapsulation of Mo nanoclusters by C_{180} lowered the energy by around $1.75–2.5\,\mathrm{eV\,atom^{-1}}$ in the cluster.

The encapsulation energy is given by:

$$\mathrm{E.E.}' \equiv \frac{E^{\mathrm{AM1}^*}(\mathrm{C}'_{180}) + E^{\mathrm{AM1}^*}(\mathrm{Mo}_n) - E^{\mathrm{AM1}^*}(\mathrm{Mo}_n@\mathrm{C}_{180})}{n}, \tag{4}$$

where $E^{\mathrm{AM1}^*}(\mathrm{Mo}_n)$ is the energy of isolated Mo_n cluster (taken from endohedral geometry without further optimisation) and all other terms have their previously defined meanings.

In terms of structural changes induced by encapsulation, there was found to be a correlation between average

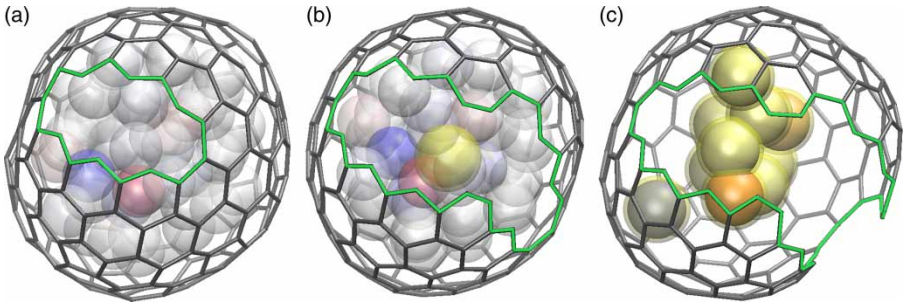

Figure 12. RHF/AM1* optimised geometries of endohedral fullerene $Mo_{(52-x)}S_x@C_{180}$ clusters: (a) $Mo_{52}@C_{180}$, (b) $Mo_{51}S@C_{180}$ and (c) $Mo_{42}S_{10}@C_{180}$. In (a) and (b), Mo atoms are represented by semi-transparent spheres, coloured (online) according to their Mulliken charges (red being negative, blue being positive) with ranges set the same for each image. In (b) and (c), sulphur atoms are highlighted by overlaying a semi-transparent yellow sphere. The fullerene defects in all three structures are highlighted in green, with full opening of fullerene cage observed in (c). As in Figure 9, bonding to Mo atoms (which terminate the dangling bonds) is not shown for clarity, and Mo atoms are also hidden in (c).

carbon–carbon bond strain and the total energy of isolated strained C_{180} molecule computed at RHF/AM1* level. The maximum average C–C bond strain was found to be around 5.5% before breakage occurs (corresponding to cluster size $n = 53$). Furthermore, Mo–Mo RDFs for $Mo_{35}@C_{180}$ (relatively unstrained) and $Mo_{51}@C_{180}$ (just before breakage) showed only a small difference; there was sharpening of nearest-neighbour peak due to confinement, but no increase in overall crystalline order.

3.4 *Endohedral $Mo_{(52-x)}S_x@C_{180}$*

In order to investigate the effect of sulphur addition on the stability of endohedral fullerene structures, preliminary results have been obtained from C_{180}-encapsulated molybdenum sulphide clusters. Since the parameter space of possible simulations for the binary $Mo_{(n-x)}S_x@C_{180}$ system is very large, it was decided to limit the study to $Mo_{(52-x)}S_x@C_{180}$ for $0 \leq x \leq 10$ in order to investigate specifically whether there was any systematic change in ordering of Mo atoms with substitution of sulphur atoms, and what effect this may have on the breakage of the fullerene π-system. As described above in Section 3.3, for $Mo_{53}@C_{180}$ shown in Figure 9(c), the fullerene cage is partially ruptured, compared with the presence of two smaller isolated 6–6 defects in the $Mo_{51}@C_{180}$ cluster, Figure 9(b). The structure of $Mo_{52}@C_{180}$ cluster, shown in Figure 12(a), displays a rupture of intermediate size, but when a single Mo atom is transformed to S, the rupture is immediately enlarged, Figure 12(b). Since the degree of polarity of the metal atoms between Figure 12(a),(b) is relatively unchanged, it is likely that this effect is simply due to the increased size of the S atom relative to a Mo atom. As in the case of a freestanding cluster of $Mo_{51}S$, the S atom is preferentially contained in the interior of the Mo cluster, rather than close to the surface. As successively more Mo atoms are transformed to S, the size of the fullerene rupture increases slightly but the distribution of S atoms tends to remain closer to the interior of the encapsulated particle (see Figure 12(c), where Mo atoms are hidden for clarity) rather than near the site of the rupture. From these albeit limited results, we can nevertheless conclude that the metal atoms play the dominant role in stabilising the edges of a broken fullerene structure, with substituted non-metal atoms influencing the structure via a secondary steric affect. However, a more conclusive investigation would require the study of much larger catalyst particles, and further studies are underway.

4. Conclusions

For the first time, SEMO calculations using the AM1* Hamiltonian have been used to study the structure and energetics of freestanding and fullerene-encapsulated Mo nanoclusters. It was observed that freestanding nanoclusters of Mo_n and $Mo_{(n-x)}X_x$ are always amorphous for $x < 35$, where X = {O, N, S}. In general, the incorporation of chalcogens lowers the binding energy of cluster, although some small increases seen for smaller x when chalcogen atoms move to surface. There is reasonable quantitative agreement between AM1* geometries and energies when compared with B3LYP using a minimal basis set. In all cases, encapsulation of Mo_n or $Mo_{(n-x)}X_x$, where X = {O, N, S}, nanoclusters by a C_{180} molecule lowers energy by around 1.75–2.5 eV atom^{-1} in cluster. This is due to stabilisation by interaction between d-electrons of Mo and the C_{180} π-system, leading to formation of defects by attack at 6–6 bonds. Eventually, the C_{180} cage opens, with corresponding increase in binding energy due to release of strain in fullerene. No systematic change in ordering of Mo atoms was seen on substitution of S species, but further investigations using larger nanoparticles are underway. Other transition metal catalysts (such as Ni, Co, Fe), and effects of magnetism should be considered in future studies.

Acknowledgements

JAE would like to acknowledge the award of an Invitation Fellowship (id L08536) from the Japanese Society for Promotion of Science (JSPS). Part of this work was financially supported by Grand-in-Aid for Young Scientist (a) (No. 18686017) from MEXT, Japan.

References

[1] Y.-L. Li, I.A. Kinloch, and A.H. Windle, *Direct spinning of carbon nanotube fibers from chemical vapor deposition synthesis*, Science 304 (2004), pp. 276–278.
[2] S. Maruyama, R. Kojima, Y. Miyauchi, S. Chiashi, and M. Kohno, *Low-temperature synthesis of high-purity single-walled carbon nanotubes from alcohol*, Chem. Phys. Lett. 360 (2002), pp. 229–234.
[3] M. Motta, A. Moisala, I.A. Kinloch, and A.H. Windle, *High performance fibres from 'Dog bone' carbon nanotubes*, Adv. Mat. 19 (2007), pp. 3721–3726.
[4] L. Ci, Z. Rao, Z. Zhou, D. Tang, X. Yan, Y. Liang, D. Liu, H. Yuan, W. Zhou, G. Wang et al., *Double wall carbon nanotubes promoted by sulfur in a floating iron catalyst CVD system*, Chem. Phys. Lett. 359 (2002), pp. 63–67.
[5] P. Winget, A.H.C. Horn, C. Selcuki, B. Martin, and T. Clark, *AM1* parameters for phosphorus, sulfur and chlorine*, J. Mol. Model. 9 (2003), pp. 408–414.
[6] *Materials Studio Modelling Environment*, v. 4.2 Accelrys Inc., San Diego, 2007.
[7] A. Thess, R. Lee, P. Nikolaev, H.J. Dai, P. Petit, J. Robert, C.H. Xu, Y.H. Lee, S.G. Kim, A.G. Rinzler et al., *Crystalline ropes of metallic carbon nanotubes*, Science 273 (1996), pp. 483–487.
[8] C. Journet, W.K. Maser, P. Bernier, A. Loiseau, M.L. delaChapelle, S. Lefrant, P. Deniard, R. Lee, and J.E. Fischer, *Large-scale production of single-walled carbon nanotubes by the electric-arc technique*, Nature 388 (1997), pp. 756–758.
[9] P. Nikolaev, M.J. Bronikowski, R.K. Bradley, F. Rohmund, D.T. Colbert, K.A. Smith, and R.E. Smalley, *Gas-phase catalytic growth of single-walled carbon nanotubes from carbon monoxide*, Chem. Phys. Lett. 313 (1999), pp. 91–97.

[10] Y. Murakami, S. Chiashi, Y. Miyauchi, M.H. Hu, M. Ogura, T. Okubo, and S. Maruyama, *Growth of vertically aligned single-walled carbon nanotube films on quartz substrates and their optical anisotropy*, Chem. Phys. Lett. 385 (2004), pp. 298–303.

[11] K. Hata, D.N. Futaba, K. Mizuno, T. Namai, M. Yumura, and S. Iijima, *Water-assisted highly efficient synthesis of impurity-free single-waited carbon nanotubes*, Science 306 (2004), pp. 1362–1364.

[12] A. Loiseau, X. Blasé, J.-C. Charlier, P. Gadelle, C. Journet, C. Laurent, and A. Peigney, *Synthesis methods and growth mechanisms*, Lect. Notes Phys. 677 (2006), pp. 49–130.

[13] D.N. Futaba, K. Hata, T. Namai, T. Yamada, K. Mizuno, Y. Hayamizu, M. Yumura, and S. Iijima, *84% Catalyst activity of water-assisted growth of single walled carbon nanotube forest characterization by a statistical and macroscopic approach*, J. Phys. Chem. B 110 (2006), pp. 8035–8038.

[14] K. Koziol, J. Vilatela, A. Moisala, M. Motta, P. Cunniff, M. Sennett, and A. Windle, *High-performance carbon nanotube fiber*, Science 318 (2007), pp. 1892–1895.

[15] G. Lolli, L.A. Zhang, L. Balzano, N. Sakulchaicharoen, Y.Q. Tan, and D.E. Resasco, *Tailoring (n,m) structure of single-walled carbon nanotubes by modifying reaction conditions and the nature of the support of CoMo catalysts*, J. Phys. Chem. B 110 (2006), pp. 2108–2115.

[16] R.S. Wagner and W.C. Ellis, *Vapor–liquid–solid mechanism of single crystal growth*, Appl. Phys. Lett. 4 (1964), pp. 89–90.

[17] R.T.K. Baker, *Catalytic growth of carbon filaments*, Carbon 27 (1989), pp. 315–323.

[18] H. Dai, A.G. Rinzler, P. Nikolaev, A. Thess, D.T. Colbert, and R.E. Smalley, *Single-wall carbon nanotubes produced by metal-catalyzed disproportionation of carbon monoxide*, Chem. Phys. Lett. 260 (1996), pp. 471–475.

[19] Y. Zhang, Y. Li, W. Kim, D. Wang, and H. Dai, *Imaging as-grown single-walled carbon nanotubes originated from isolated catalytic nanoparticles*, Appl. Phys. Mater. Sci. Process. 74 (2002), pp. 325–328.

[20] Y. Shibuta and S. Maruyama, *Molecular dynamics simulation of formation process of single-walled carbon nanotubes by CCVD method*, Chem. Phys. Lett. 382 (2003), pp. 381–386.

[21] Y. Shibuta and S. Maruyama, *A molecular dynamics study of the effect of a substrate on catalytic metal clusters in nucleation process of single-walled carbon nanotubes*, Chem. Phys. Lett. 437 (2007), pp. 218–223.

[22] J.E. Herrera, L. Balzano, A. Borgna, W.E. Alvarez, and D.E. Resasco, *Relationship between the structure/composition of Co-Mo catalysts and their ability to produce single-walled carbon nanotubes by CO disproportionation*, J. Catal. 204 (2001), pp. 129–145.

[23] A.D. Lan, Y. Zhang, X.Y. Zhang, Z. Iqbal, and H. Grebel, *Is molybdenum necessary for the growth of single-wall carbon nanotubes from CO?* Chem. Phys. Lett. 379 (2003), pp. 395–400.

[24] M. Yudasaka, Y. Kasuya, F. Kokai, K. Takahashi, M. Takizawa, S. Bandow, and S. Iijima, *Causes of different catalytic activities of metals in formation of single-wall carbon nanotubes*, Appl. Phys. Mater. Sci. Process. 74 (2002), pp. 377–385.

[25] E. Flahaut, A. Peigney, W.S. Bacsa, R.R. Bacsa, and C. Laurent, *CCVD synthesis of carbon nanotubes from (Mg,Co,Mo)O catalysts: Influence of the proportions of cobalt and molybdenum*, J. Mater. Chem. 14 (2004), pp. 646–653.

[26] M.H. Hu, Y. Murakami, M. Ogura, S. Maruyama, and T. Okubo, *Morphology and chemical state of Co-Mo catalysts for growth of single-walled carbon nanotubes vertically aligned on quartz substrates*, J. Catal. 225 (2004), pp. 230–239.

[27] S. Noda, H. Sugime, T. Osawa, Y. Tsuji, S. Chiashi, Y. Murakami, and S. Maruyama, *A simple combinatorial method to discover Co-Mo binary catalysts that grow vertically aligned single-walled carbon nanotubes*, Carbon 44 (2006), pp. 1414–1419.

[28] S. Noda, K. Hasegawa, H. Sugime, K. Kakehi, Z. Zhang, S. Maruyama, and Y. Yamaguchi, *Millimeter-thick single-walled carbon nanotube forests: Hidden role of catalyst support*, Jpn. J. Appl. Phys. 46 (2007), pp. L399–L401.

[29] Y. Shibuta and S. Maruyama, *Bond-order potential for transition metal carbide cluster for the growth simulation of a single-walled carbon nanotube*, Comput. Mater. Sci. 39 (2007), pp. 842–848.

[30] F. Ding, A. Rosen, and K. Bolton, *Molecular dynamics study of the catalyst particle size dependence on carbon nanotube growth*, J. Chem. Phys. 121 (2004), pp. 2775–2779.

[31] J.Y. Raty, F. Gygi, and G. Galli, *Growth of carbon nanotubes on metal nanoparticles: A microscopic mechanism from* ab initio *molecular dynamics simulations*, Phys. Rev. Lett. 95 (2005), 096103.

[32] J.C. Charlier, H. Amara, and P. Lambin, *Catalytically assisted tip growth mechanism for single-wall carbon nanotubes*, Acs Nano 1 (2007), pp. 202–207.

[33] J. Gavillet, A. Loiseau, C. Journet, F. Willaime, F. Ducastelle, and J.C. Charlier, *Root-growth mechanism for single-wall carbon nanotubes*, Phys. Rev. Lett. 8727 (2001), 275504.

[34] H. Amara, C. Bichara, and F. Ducastelle, *Formation of carbon nanostructures on nickel surfaces: A tight-binding grand canonical Monte Carlo study*, Phys. Rev. B 73 (2006).

[35] A.R. Leach, *Molecular Modelling: Principles and Applications*, 2nd ed., Prentice-Hall, Englewood Cliffs, 2001.

[36] Y. Shibuta and J.A. Elliott, *A molecular dynamics study of the carbon–catalyst interaction energy for multi-scale modelling of single wall carbon nanotube growth*, Chem. Phys. Lett. 427 (2006), pp. 365–370.

[37] C.L. Cleveland, W.D. Luedtke, and U. Landman, *Melting of gold clusters*, Phys. Rev. B 60 (1999), pp. 5065–5077.

[38] Y. Dong and M. Springborg, *Unbiased determination of structural and electronic properties of gold clusters with up to 58 atoms*, J. Phys. Chem. C 111 (2007), pp. 12528–12535.

[39] D. Alamanova, V.G. Grigoryan, and M. Springborg, *Theoretical study of the structure and energetics of silver clusters*, J. Phys. Chem. C 111 (2007), pp. 12577–12587.

[40] F. Ding, A. Rosen, S. Curtarolo, and K. Bolton, *Modeling the melting of supported clusters*, Appl. Phys. Lett. 88 (2006), p. 133110.

[41] H.K. Kim, S.H. Huh, J.W. Park, J.W. Jeong, and G.H. Lee, *The cluster size dependence of thermal stabilities of both molybdenum and tungsten nanoclusters*, Chem. Phys. Lett. 354 (2002), pp. 165–172.

[42] S.H. Huh, H.K. Kim, J.W. Park, and G.H. Lee, *Critical cluster size of metallic Cr and Mo nanoclusters*, Phys. Rev. B 62 (2000), pp. 2937–2943.

[43] Y. Shibuta and T. Suzuki, *Melting and nucleation of iron nanoparticles: A molecular dynamics study*, Chem. Phys. Lett. 445 (2007), pp. 265–270.

[44] F. Baletto and R. Ferrando, *Structural properties of nanoclusters: Energetic, thermodynamic, and kinetic effects*, Rev. Modern Phys. 77 (2005), pp. 371–423.

[45] J.A. Alonso, *Electronic and atomic structure, and magnetism of transition-metal clusters*, Chem. Rev. 100 (2000), pp. 637–677.

[46] D.J. Wales and J.P.K. Doye, *Global optimization by basin-hopping and the lowest energy structures of Lennard-Jones clusters containing up to 110 atoms*, J. Phys. Chem. A 101 (1997), pp. 5111–5116.

[47] J.P.K. Doye and D.J. Wales, *Global minima for transition metal clusters described by Sutton–Chen potentials*, New J. Chem. 22 (1998), pp. 733–744.

[48] L.X. Zhan, J.Z.Y. Chen, W.K. Liu, and S.K. Lai, *Asynchronous multicanonical basin hopping method and its application to cobalt nanoclusters*, J. Chem. Phys. 122 (2005), pp. 1–9.

[49] M.V. Bollinger, K.W. Jacobsen, and J.K. Norskov, *Atomic and electronic structure of MoS2 nanoparticles*, Phys. Rev. B 67 (2003), 085410.

[50] G. Seifert, J. Tamuliene, and S. Gemming, *MonS2n + x clusters-magic numbers and platelets*, Comput. Mater. Sci. 35 (2006), pp. 316–320.

[51] P. Murugan, V. Kumar, Y. Kawazoe, and N. Ota, *Bonding nature and magnetism in small MoX2 (X = O and S) clusters – a comparative study by first principles calculations*, Chem. Phys. Lett. 423 (2006), pp. 202–207.

[52] S. Gemming, J. Tamuliene, G. Seifert, N. Bertram, Y.D. Kim, and G. Gantefor, *Electronic and geometric structures of MoxSy and*

WxSy (x = 1, 2, 4; y = 1-12) clusters, Appl. Phys. Mater. Sci. Process. 82 (2006), pp. 161–166.
[53] J.V. Lauritsen, J. Kibsgaard, S. Helveg, H. Topsoe, B.S. Clausen, E. Laegsgaard, and F. Besenbacher, *Size-dependent structure of MoS2 nanocrystals*, Nat. Nanotechnol. 2 (2007), pp. 53–58.
[54] P. Murugan, V. Kumar, Y. Kawazoe, and N. Ota, *Understanding the structural stability of compound Mo-S clusters at sub-nanometer level*, Mater. Transact. 48 (2007), pp. 658–661.
[55] P. Murugan, V. Kumar, Y. Kawazoe, and N. Ota, Ab initio *study of structural stability of Mo-S clusters and size specific stoichiometries of magic clusters*, J. Phys. Chem. A 111 (2007), pp. 2778–2782.
[56] T.S. Li and G.L. Galli, *Electronic properties of MOS2 nanoparticles*, J. Phys. Chem. C 111 (2007), pp. 16192–16196.
[57] M.J.S. Dewar and W. Thiel, *Ground-states of molecules. 38. MNDO method – approximations and parameters*, J. Am. Chem. Soc. 99 (1977), pp. 4899–4907.
[58] M.J.S. Dewar and W. Thiel, *Ground-states of molecules. 39. MNDO results for molecules containing hydrogen, carbon, nitrogen, and oxygen*, J. Am. Chem. Soc. 99 (1977), pp. 4907–4917.
[59] T. Bredow and K. Jug, *Theory and range of modern semiempirical molecular orbital methods*, Theor. Chem. Acc. 113 (2005), pp. 1–14.
[60] J.B. Foresman and A. Frisch, *Exploring Chemistry with Electronic Structure Methods*, 2nd ed., Gaussian Inc., Pittsburgh, 1996.
[61] C.T. Lee, W.T. Yang, and R.G. Parr, *Development of the Colle-Salvetti correlation-energy formula into a functional of the electron-density*, Phys. Rev. B 37 (1988), pp. 785–789.
[62] A.D. Becke, *Density-functional thermochemistry. 3. The role of exact exchange*, J. Chem. Phys. 98 (1993), pp. 5648–5652.
[63] A.D. Bacon and M.C. Zerner, *An intermediate neglect of differential overlap theory for transition metal complexes: Fe, Co and Cu chlorides*, Theor. Chim. Acta 52 (1979), pp. 21–54.
[64] W. Thiel and A.A. Voityuk, *Extension of the MNDO formalism to d-orbitals – integral approximations and preliminary numerical results*, Theor. Chim. Acta 81 (1992), pp. 391–404.
[65] A.A. Voityuk and N. Rosch, *AM1/d parameters for molybdenum*, J. Phys. Chem. A 104 (2000), pp. 4089–4094.
[66] P. Winget, C. Selcuki, A.H.C. Horn, B. Martin, and T. Clark, *Towards a "next generation" neglect of diatomic differential overlap based semiempirical molecular orbital technique*, Theor. Chem. Acc. 110 (2003), pp. 254–266.
[67] P. Winget and T. Clark, *AM1* parameters for aluminum, silicon, titanium and zirconium*, J. Mol. Model. 11 (2005), pp. 439–456.
[68] J.J.P. Stewart, *Optimization of parameters for semiempirical methods V: Modification of NDDO approximations and application to 70 elements*, J. Mol. Model. 13 (2007), pp. 1173–1213.
[69] D. Young, *Computational Chemistry: A Practical Guide for Applying Techniques to Real World Problems*, Wiley Interscience, New York, 2001.
[70] M.J. Frisch, G.W. Trucks, H.B. Schlegel, G.E. Scuseria, M.A. Robb, J.R. Cheeseman, J.A.M.T. Vreven, Jr., K.N. Kudin, J.C. Burant, J.M. Millam et al. *Guassian 03*, Gaussian Inc., Wallingford, CT, 2004.
[71] D.J. Wales, J.P.K. Doye, A. Dullweber, M.P. Hodges, F.Y. Naumkin, F. Calvo, J. Hernández-Rojas, and T.F. Middleton, *The Cambridge cluster database*, URL http://www-wales.ch.cam.ac.uk/CCD.html (2007).
[72] M.S. Motta, A. Moisala, I.A. Kinloch, A.H. Windle, *The role of sulphur in the synthesis of carbon nanotubes by chemical vapour deposition at high temperatures*, J. Nanosci. Nanotech. 8 (2008), pp. 2442–2449.
[73] M. Saunders, H.A. Jimenezvazquez, R.J. Cross, and R.J. Poreda, *Stable compounds of helium and neon – He@C60 and Ne@C60*, Science 259 (1993), pp. 1428–1430.
[74] M. Saunders, H.A. Jimenezvazquez, R.J. Cross, S. Mroczkowski, M.L. Gross, D.E. Giblin, and R.J. Poreda, *Incorporation of helium, neon, argon, krypton and xenon into fullerenes using high-pressure*, J. Am. Chem. Soc. 116 (1994), pp. 2193–2194.
[75] J. Lu, L.X. Ge, X.W. Zhang, and X.G. Zhao, *Electronic structures of endohedral Sr@C-60 Ba@C-60, Fe@C-60 and Mn@C-60*, Modern Phys. Lett. B 13 (1999), pp. 97–101.
[76] J. Lu, X.W. Zhang, and X.G. Zhao, *Electronic structures of endohedral Ca@C-60, SC@C-60 and Y@C-60*, Solid State Commun. 110 (1999), pp. 565–568.
[77] J. Lu, X.W. Zhang, and X.G. Zhao, *Electronic structures of endohedral N@C-60, O@C-60 and F@C-60*, Chem. Phys. Lett. 312 (1999), pp. 85–90.
[78] J.C. Greer, *The atomic nature of endohedrally encapsulated nitrogen N@C-60 studied by density functional and Hartree-Fock methods*, Chem. Phys. Lett. 326 (2000), pp. 567–572.
[79] W. Humphrey, A. Dalke, and K. Schulten, *VMD: Visual molecular dynamics*, J. Mol. Graph. 14 (1996), pp. 33–38.
[80] C.Y. Moon, Y.S. Kim, E.C. Lee, Y.G. Jin, and K.J. Chang, *Mechanism for oxidative etching in carbon nanotubes*, Phys. Rev. B 65 (2002), 155401.